

Self-Powered and Broadband Lead-Free Inorganic Perovskite Photodetector with High Stability

*Original*

Self-Powered and Broadband Lead-Free Inorganic Perovskite Photodetector with High Stability / Liu, D.; Yu, B. -B.; Liao, M.; Jin, Z.; Zhou, L.; Zhang, X.; Wang, F.; He, H.; Gatti, T.; He, Z.. - In: ACS APPLIED MATERIALS & INTERFACES. - ISSN 1944-8244. - 12:27(2020), pp. 30530-30537. [10.1021/acsami.0c05636]

*Availability:*

This version is available at: 11583/2977480 since: 2023-03-30T10:38:55Z

*Publisher:*

American Chemical Society

*Published*

DOI:10.1021/acsami.0c05636

*Terms of use:*

This article is made available under terms and conditions as specified in the corresponding bibliographic description in the repository

*Publisher copyright*

ACS postprint/Author's Accepted Manuscript

This document is the Accepted Manuscript version of a Published Work that appeared in final form in ACS APPLIED MATERIALS & INTERFACES, copyright © American Chemical Society after peer review and technical editing by the publisher. To access the final edited and published work see <http://dx.doi.org/10.1021/acsami.0c05636>.

(Article begins on next page)

# Self-Powered and Broadband Lead-Free Inorganic Perovskite Photodetector with High Stability

Di Liu,<sup>#</sup> Bin-Bin Yu,<sup>#</sup> Min Liao, Zhixin Jin, Liang Zhou, Xiuxing Zhang, Fengyun Wang,<sup>\*</sup> Hongtao He, Teresa Gatti, and Zhubing He<sup>\*</sup>

Authors

Di Liu – Department of Materials Science and Engineering, Shenzhen Key Laboratory of Full Spectral Solar Electricity Generation (FSSEG), Southern University of Science and Technology, Shenzhen 518055, Guangdong, China; College of Physics and State Key Laboratory of Bio-Fibers and Eco- Textiles, Qingdao University, Qingdao 266071, China

Bin-Bin Yu – Department of Materials Science and Engineering, Shenzhen Key Laboratory of Full Spectral Solar Electricity Generation (FSSEG), Southern University of Science and Technology, Shenzhen 518055, Guangdong, China; Academy for Advanced Interdisciplinary Studies, Southern University of Science and Technology (SUSTech), Shenzhen 518055, China

Min Liao – Department of Materials Science and Engineering, Shenzhen Key Laboratory of Full Spectral Solar Electricity Generation (FSSEG), Southern University of Science and Technology, Shenzhen 518055, Guangdong, China

Zhixin Jin – Department of Materials Science and Engineering, Shenzhen Key Laboratory of Full Spectral Solar Electricity Generation (FSSEG), Southern University of Science and Technology, Shenzhen 518055, Guangdong, China

Liang Zhou – Department of Physics, Southern University of Science and Technology, Shenzhen 518055, Guangdong, P. R. China

Xiuxing Zhang – Department of Materials Science and Engineering, Shenzhen Key Laboratory of Full Spectral Solar Electricity Generation (FSSEG), Southern University of Science and Technology, Shenzhen 518055, Guangdong, China

Hongtao He – Department of Physics, Southern University of Science and Technology, Shenzhen 518055, Guangdong, P. R. China; [orcid.org/0000-0001-6748-874X](https://orcid.org/0000-0001-6748-874X)

Teresa Gatti – Institute of Physical Chemistry and Center for Materials Research (LaMa), Justus Liebig University, 35392 Giessen, Germany

**ABSTRACT:** Metal halide perovskite materials have opened up a great opportunity for high-performance optoelectronic devices owing to their extraordinary optoelectronic properties. More than lead halide ones, stable and nontoxic bismuth halide perovskites exhibit more promise in their future commercialization. In this work, we developed for the first time photodetectors based on full-inorganic  $\text{Cs}_3\text{Bi}_2\text{I}_9-x\text{Br}_x$  perovskites and modulate their performance by varying  $x$  in the composition systematically. Among those self-powered photodetectors, those based on  $\text{Cs}_3\text{Bi}_2\text{I}_6\text{Br}_3$  shows the best performance with excellent photosensitivity of  $4.1 \times 10^4$  at zero bias as well as the responsivity and detectivity reaching 15 mA/W and  $4.6 \times 10^{11}$  Jones, respectively. More strikingly, the full-inorganic perovskite photodetectors exhibit excellent stability in the ambient environment and can maintain over 96% of the initial value after 100 days owing to the high stability of the core perovskite film. The paper definitely paves an alternative and promising strategy for the design of future commercial photodetectors that are self-powered, stable, nontoxic, etc.

**KEYWORDS:** bismuth halide perovskites, composition engineering, full inorganic, photodetector, self-powered, stability

## INTRODUCTION

Among the important optoelectronic devices, UV detection plays an essential role in biological analysis, space exploration, environmental sensors, and UV irradiation detections.<sup>1-3</sup> In the past few decades, UV photodetectors with wide-band-gap semiconductors have been studied extensively owing to their suitable direct band gap and low cost, such as (Al) GaN, AlN,<sup>4</sup> ZnO,<sup>5-9</sup> TiO<sub>2</sub>,<sup>10-12</sup> WO<sub>3</sub>,<sup>13</sup> etc. However, Group III nitrides are usually synthesized via relatively expensive approaches such as vapor-liquid-solid or epitaxy, which accounts for their high<sup>14,15</sup> cost and hence hampers their commercial application. On the other hand, those photodetectors based on metal oxide suffer from persistent photoconductivity (PPC) caused by the surface and bulk deep-level defects,<sup>16,17</sup> resulting in long response tails. Depending on the three-terminal thin-film transistor (TFT) device structure design with amorphous oxide as a gate, Jeon et al. solved the problem of PPC to a large extent by developing gated semiconductor photo thin-film transistor (photo-TFT), accelerating the recombination of electrons and ionized oxygen vacancies with the application of a short (10 ns) voltage pulse to these devices.<sup>18</sup> However, the complicated three-terminal TFT-based devices suffer from high fabrication cost and narrow operation window, which exhibits the demand to develop facile two-terminal UV detectors using novel optoelectronic materials.

On the other hand, for the past decade, lead halide perovskite materials have attracted extensive attention owing to their unique optoelectronic properties including high carrier mobility, high optical absorption coefficient, and long carrier diffusion length<sup>19-21</sup> and have achieved significant progress in photovoltaic devices,<sup>22-24</sup> photodetectors,<sup>25-27</sup> light-emitting diodes,<sup>28</sup> and so on based on these photodetectors. Interestingly, most photodetectors based on those perovskite materials have a fast response speed.<sup>26,29</sup> For example, the optimized CsPbIBr<sub>2</sub>-based photodetector constructed by Bao et al. shows a measured detectable limit of around 21.5 pW/cm<sup>2</sup> and a short response time of 20 ns,<sup>29</sup> which exhibit the huge potential of the perovskite-based photodetectors for optical communication. Because most lead-based and tin-based perovskite materials have narrow band gaps and their effective photon-to-current responses are limited in the visible and infrared region,<sup>27,29</sup> the response to the purple and ultraviolet light is really poor and it cannot realize a broadband detection covering UV light.<sup>30</sup> Moreover, those perovskite materials suffer from severe instability, which remains a big obstacle in their commercialization,<sup>31</sup> in addition to the toxicity issue, especially for lead halide perovskite materials. To address the above crucial concerns, bismuth halide perovskites were introduced to construct stable and environmental-friendly UV-vis photodetector devices because of their wide band gap, nontoxicity, and high stability.<sup>32-34</sup> Generally speaking, all-inorganic halide perovskites show higher stability than the organic-inorganic hybrid ones.<sup>35</sup> Cs<sub>3</sub>Bi<sub>2</sub>I<sub>9</sub>, as an all-inorganic lead-free perovskite, has a suitable optical band gap for UV-vis broadband photodetectors along with superior stability and structure and optoelectronic properties that can be tuned by changing halide contents.<sup>36,37</sup> For instance, replacing some I by Br can lead to interesting phase changes and tune their band gaps and herein modulate the photoresponse to UV-vis light.<sup>37-39</sup> As far as we know, Cs Bi I Br -based photo- 3 29-x x detectors are hardly studied and the performance of the devices based on them deserves to be explored.

In this work, the Cs<sub>3</sub>Bi<sub>2</sub>I<sub>9-x</sub>Br<sub>x</sub> perovskite films were successfully synthesized and photodetectors based on them were studied systematically in a device configuration of ITO/ PEDOT:PSS/Cs<sub>3</sub>Bi<sub>2</sub>I<sub>9-x</sub>Br<sub>x</sub>/C<sub>60</sub>/BCP/Ag by varying x from 0 to 9. The crystallinity, film morphology, and optoelectronic properties of that series of Cs<sub>3</sub>Bi<sub>2</sub>I<sub>9-x</sub>Br<sub>x</sub> perovskite films were characterized systematically, and photodetectors based on them show typically self-power; the key device-performance indexes were also investigated in detail. Among them, the Cs<sub>3</sub>Bi<sub>2</sub>I<sub>6</sub>Br<sub>3</sub>-based photodetectors show outstanding device performance. Its photosensitivity (S) reaches  $4.1 \times 10^4$  at zero bias and the responsivity and detectivity reach 15 mA/W and  $4.6 \times 10^{11}$  Jones, respectively. Besides, the response and decay duration of the device are as low as 40.7 and 27.1 ms, respectively. Moreover, the unencapsulated Cs<sub>3</sub>Bi<sub>2</sub>I<sub>6</sub>Br<sub>3</sub>-based devices show excellent stability such that its photocurrent remains over 95% after 100 days of exposure in the ambient environment.

## RESULTS AND DISCUSSION

In his work, a series of  $\text{Cs}_3\text{Bi}_2\text{I}_{9-x}\text{Br}_x$  thin films ( $x = 0, 1, 2, 3, 4, 5, 6, 7, 8, 9$ ) were successively prepared via a typical spin-coating method. The X-ray diffraction (XRD) measurement was carried out to investigate the crystalline quality and phase transition of those Bi-based perovskite films (shown in Figures 1a and S1). As Figure S1 shows, the  $\text{Cs}_3\text{Bi}_2\text{I}_9$  film has a typical  $\text{P6}_3/\text{mmc}$  phase (JCPDS 23-0847), while the  $\text{Cs}_3\text{Bi}_2\text{I}_6\text{Br}_3$  film belongs to the  $\text{P3m}$  phase (JCPDS 44-0714), which has been well analyzed in the previous report.<sup>37,38</sup> Similarly, the  $\text{Cs Bi I Br}$  films gradually change from the  $\text{P6}$  phase of  $3/29-x/3 \text{ Cs}_3\text{Bi}_2\text{I}_9$  (dark yellow line) to the  $\text{P3m}$  phase of  $\text{Cs}_3\text{Bi}_2\text{I}_6\text{Br}_3$  (red line) as the value of  $x$  increases from 0 to 9.<sup>37</sup> As our previous paper declares,<sup>37</sup> the kink point turns up at  $x = 3$ . That is because three Br ions are required to occupy the bridging position in the cell and hence form a stable mixed structure.<sup>38,39</sup> Notably, the highest intensity of the (006) peak in the XRD pattern of those  $\text{Cs}_3\text{Bi}_2\text{I}_6\text{Br}_3$  films demonstrates the best crystallinity among the series of films. The enhanced crystallinity definitely leads to improved optoelectronic properties. In the evolution with the increase of  $x$ , the obvious red shift of the main peaks can be ascribed to the reduced lattice constant caused by incorporating Br into the iodine perovskite structure, which is consistent with the previous reports.<sup>37-39</sup>

Figure S2 shows the typical optical photos of the  $\text{Cs}_3\text{Bi}_2\text{I}_{9-x}\text{Br}_x$  films. Their colors turn deeper when  $x$  increases from 0 to 3 except for  $\text{Cs}_3\text{Bi}_2\text{I}_8\text{Br}_1$  and become lighter and lighter, which is clearly in accordance with the evolution of their structure as discussed above and also well discussed.<sup>37</sup> Among them,  $\text{Cs}_3\text{Bi}_2\text{I}_6\text{Br}_3$  is the deepest one due to the band gap shrinking caused by the phase transition from  $\text{P6}_3$  to  $\text{P3m}$ .<sup>37</sup> Some typical UV-vis absorption spectra are shown in Figure 1b, while those of all the  $\text{Cs}_3\text{Bi}_2\text{I}_{9-x}\text{Br}_x$  film are collected in Figure S3. Although we reported already this absorption phenomenon,<sup>37</sup> it still should be noted again that  $\text{Cs}_3\text{Bi}_2\text{I}_6\text{Br}_3$  shows the reddest absorption edge of ca. 590 nm other than  $\text{Cs}_3\text{Bi}_2\text{I}_9$ . Also, the absorption edge of those samples has a successive blue shift when  $x$  changes from 3 to 9. The law is consistent with the color change trend of their corresponding photographs (Figure S2). The absorption onset of the  $\text{Cs}_3\text{Bi}_2\text{I}_{9-x}\text{Br}_x$  film has an obvious red shift when the  $x$  increases to 3 and then shifts back to ca. 465 nm (black line) as the Br/I increases to 9/0. Among them, the weaker absorption of the  $\text{Cs}_3\text{Bi}_2\text{I}_9$  and  $\text{Cs}_3\text{Bi}_2\text{I}_8\text{Br}_1$  films may suffer from the low crystallinity of mixed phases and poor film coverage.<sup>37,38</sup>

As we know, the film morphology plays an important role in device fabrication and herein performance. The typical scanning electron microscopy (SEM) images of all of the  $\text{Cs}_3\text{Bi}_2\text{I}_{9-x}\text{Br}_x$  perovskite films are shown in Figure 1c(l). As the typical hexagonal phase ( $\text{P6}_3$ ),  $\text{Cs}_3\text{Bi}_2\text{I}_9$  shows cross-composed hexagonal plates in morphology.  $\text{P6}_3/\text{mmc}$  hexagonal phase dominates  $\text{Cs}_3\text{Bi}_2\text{I}_9$  and  $\text{Cs}_3\text{Bi}_2\text{I}_8\text{Br}_1$  films and has zero-dimensional structure,<sup>38,39</sup> resulting in the growth of cross-grown hexagonal nanosheets in morphology and similar to previous works.<sup>37,38,40-42</sup> With I is replaced by Br in the initial stage, the shape of plates changes from hexagonal to circle and the vertical growth turns weak. When  $x$  reaches 3, the large size plates merge with each other and become a dense and flat film along with the disappearance of gross nanorods and separate cross-grown flakes. This unambiguously proves the phase transition at  $x = 3$  (Figure S1) and the evolution of absorption spectra with the increase of  $x$  (Figures S2 and S3). As we

know, the flat and compact film is the prerequisite for device fabrication. So, it is difficult for us to anticipate the good performance of devices based on  $\text{Cs}_3\text{Bi}_2\text{I}_{9-x}\text{Br}_x$  with  $x = 0, 1$ , and 2. Owing to  $\text{P3m}$  phase structure, the films are composed of different sized particles and turn flat (Figure 1f-l), which affords successful device fabrication. The variation in the film morphology can be ascribed to the changing content of Br in the composition.

Based on those flat and compact films, photodetectors on them were fabricated with a typical device configuration of ITO/PEDOT:PSS/ $\text{Cs}_3\text{Bi}_2\text{I}_{9-x}\text{Br}_x/\text{C}_{60}/\text{BCP}/\text{Ag}$  (Figure 2a). The ultraviolet photoelectron spectroscopy (UPS) and Tauc plots of the UV-vis absorption spectra were performed to determine the electronic structure of the  $\text{Cs}_3\text{Bi}_2\text{I}_6\text{Br}_3$  film. From the onset of the UPS spectra (Figure S5a), the work functions of the  $\text{Cs}_3\text{Bi}_2\text{I}_6\text{Br}_3$  film are determined to be -5.02 eV. Deduced from the tail of UPS spectra (Figure S5b), the corresponding valence band maximum (VBM) position is located at -5.72 eV. The Tauc plot of the absorption spectra of the  $\text{Cs}_3\text{Bi}_2\text{I}_6\text{Br}_3$  film reveals its band gap to be 2.07 eV (Figure S4). Also, then the VBM and the conduction band minimum (CBM) of the  $\text{Cs}_3\text{Bi}_2\text{I}_6\text{Br}_3$  film can be determined to be -5.72 and -3.65 eV, respectively. The composed band-level diagram of a device based on the  $\text{Cs}_3\text{Bi}_2\text{I}_6\text{Br}_3$  film is shown in Figure 2b. The other end of the band gap of the series of films is 2.68 eV, belonging to  $\text{Cs}_3\text{Bi}_2\text{I}_9$ , which means this device configuration can cover the evaluation of all those  $\text{Cs}_3\text{Bi}_2\text{I}_{9-x}\text{Br}_x$  films, although they have little difference in the band-level offset. Figure 2c shows the variation law of photocurrent ( $I_{\text{ph}}$ ) and open-circuit voltage ( $V_{\text{oc}}$ ) with the change of  $x$  in  $\text{Cs}_3\text{Bi}_2\text{I}_{9-x}\text{Br}_x$ , which are extracted from the corresponding current-voltage curves of those devices

tested under different bias voltages, as shown in Figure S6. Both  $V_{oc}$  and  $I_{ph}$  of those devices increase along with the decrease of  $x$ . The correlating relationship between  $V_{oc}$  and  $I_{ph}$  can be attributed to the natural relationship between them,  $V_{oc} = k \ln(I_{ph}/I_d)$ , where  $I_d$  is the dark current.<sup>43</sup> The  $Cs_3Bi_2I_6Br_3$ -based device shows the best performance (Figure 2c), which can be ascribed to high crystallinity and compactness of the film obtained shown in the XRD and the UV absorption spectra.<sup>44</sup>

As the key performance index, responsivity ( $R_\lambda$ ) reflects the spectrum-dependent response efficiency of a photodetector to an optical signal and can be express as eq 1

$$\frac{I_{ph} - I_d}{P(1)}$$

To further test the device performance, Figure 3a shows dark current and photocurrent (under the white light with an intensity of 75 mW/cm<sup>2</sup>) of the  $Cs_3Bi_2I_6Br_3$ -based device in a forward scan between -0.5 and 0.75 V. The dark current is as low as 0.11 nA at zero bias, which demonstrates our  $Cs_3Bi_2I_6Br_3$ -based device can detect weak light signal, especially in such a broad wavelength. It also exhibits the maximum photosensitivity ( $S$ ,  $S = (I_{ph} - I_d)/I_d$ ) of  $4.1 \times 10^4$ , at zero bias, which is comparable with the previously reported values of perovskites.<sup>33,34</sup> This  $Cs_3Bi_2I_6Br_3$  device shows a short-circuit current ( $I_{sc}$ ) of 4.5  $\mu$ A and an open-circuit voltage ( $V_{oc}$ ) 0.61 V under the illumination of the white light with an intensity of 75 mW/cm<sup>2</sup>. The corresponding dark current is 0.11 nA at an aperture area of 3.14 mm<sup>2</sup>, and the dark current density is  $3.5 \times 10^{-9}$  A/cm<sup>2</sup> under a zero bias. To examine the reproducibility of the  $Cs_3Bi_2I_6Br_3$ -based device, the photo- currents and dark currents of a batch of 12 devices were collected and are shown in Figure 3b. The former varies from 3.5 to 6.1  $\mu$ A, while the latter changes from 75 to 360 pA. The average values of the photocurrent and dark current are 145 pA and 4.7  $\mu$ A, respectively, as red and black dashed lines. This result confirms the good reproducibility of the  $Cs_3Bi_2I_6Br_3$ - based devices.

Figure 3c shows the light-density-dependent photocurrent. As we know, the photocurrent follows the equation  $I_{ph} = kP^\theta$ , where  $I_{ph}$  is the photocurrent,  $k$  is the constant at a specific wavelength,  $P_{in}$  is the incident light intensity, and the exponent  $\theta$  is found to be 0.61 for the  $Cs_3Bi_2I_6Br_3$ -based photodetector. The departure of the exponent from unity ( $0.5 < \theta < 1$ ) indicates a complex process of electron-hole generation, separation, trapping, and recombination within the device.<sup>34,45</sup> This result proves that our  $Cs_3Bi_2I_6Br_3$ -based photodetector exhibits apparent inten- sity-dependent characteristics, and a higher light intensity results in a larger photocurrent. The intensity of each wavelength slot is different for the whole spectrum, which

$$R_\lambda = \frac{I_{ph} - I_d}{P_{in}}$$

where  $I_{ph}$  is the photocurrent under light irradiation,  $I_d$  is the dark current, and  $P_{in}$  is the incident light intensity. The responsivity test was conducted under a bias voltage of 0 V and stimulated by a monochromatic light source.

The responsivity of those  $Cs_3Bi_2I_{9-x}Br_x$ -based ( $x = 3, 4, 5, 6, 7, 8, 9$ ) photodetectors are shown in Figure 2d. Beyond any questions, the  $Cs_3Bi_2I_6Br_3$ -based device shows an outstanding  $R_\lambda$  compared with the other ones. The  $R_\lambda$  intensity of the  $Cs_3Bi_2I_6Br_3$ -based device reaches 0.015 A/W around 400 nm with a broad span of nearly 100 nm, which is 10 times that of the  $Cs_3Bi_2I_5Br_4$ -based device and even 2 orders larger than that of the following five kinds of devices ( $x = 5, 6, 7, 8, 9$ ). That can be definitely attributed to high and pure crystalline, good film quality, and well-matched band-level alignment in devices. If we check those responsivity spectra carefully, as the inset shows, the peak of each spectra shifts from ca. 320 to 400 nm when  $x$  decreases from 9 to 3, which is in accordance with the optical band gap of each  $Cs_3Bi_2I_{9-x}Br_x$  material (Figure 1b). Interestingly, their detecting spectra turn broader and broader with decreasing  $x$ . Also, the optimal  $Cs_3Bi_2I_6Br_3$ -based device can detect almost the spectra from 300 to 600 nm, which is the typical visible and near-ultraviolet light. This function becomes more powerful because it is self-powered in their applications. definitely influences the detectivity of each wavelength photon. As an important parameter, the detectivity ( $D^*$ ) reflects the detection capability of a photodetector, which can be expressed as eq 2

$$R S^{1/2}$$

$$D^* = \frac{R_\lambda}{(2eI_d)^{1/2}} \quad (2)$$

where  $R_\lambda$  is the responsivity,  $I_d$  is the dark current,  $S$  is the effective area of light irradiation, and  $e$  is the value of the electronic charge. Figure 3d shows the responsivity and detectivity of the  $\text{Cs}_3\text{Bi}_2\text{I}_6\text{Br}_3$ -based photodetectors. It is obvious that the detectivity follows the change in responsivity. When the maximum responsivity ( $\sim 15$  mA/W) stays at the wavelength of 410 nm, the detectivity also turns up at this point with a value of  $4.6 \times 10^{11}$  Jones. The broad and high detectivity along the wavelength span from 300 to 600 nm exhibits its promising application in the broadband region including both near-UV and visible spectra. Especially the result of the detection of UV light shows that our  $\text{Cs}_3\text{Bi}_2\text{I}_6\text{Br}_3$ -based photodetector is competent and even superior to the traditional wide-band-gap photodetectors.<sup>8,9,15,46</sup> A summary of the main device-performance parameters of the  $\text{Cs}_3\text{Bi}_2\text{I}_6\text{Br}_3$  photodetectors is collected in Figure S7. As summarized in Table S1, the average values and the standard deviations of the photosensitivity, responsivity, and detectivity of a batch of 12  $\frac{1}{2}$   $\text{Cs}_3\text{Bi}_2\text{I}_6\text{Br}_3$  photodetectors are  $3.86 \times 10^4$  ( $1.47 \times 10^4$ ),  $13.7$   $\pm 11$

The response speed is another critical parameter of photodetectors. As shown in Figure 4a, the photocurrent of the  $\text{Cs}_3\text{Bi}_2\text{I}_6\text{Br}_3$ -based photodetector is observed to be uniform and repeatable at a zero bias with the light on/off switching radiation at an interval of 10 s under the wavelength of 375 nm, which indicates that the photodetector has no degeneracy effect with the ability to work continuously. Figure 4b,c records the rise and decay times of the  $\text{Cs}_3\text{Bi}_2\text{I}_6\text{Br}_3$ -based photodetectors, respectively. The rise time ( $\tau_r$ ) is defined as the duration of the photocurrent increasing from 10 to 90% of the maximum photocurrent, while the decay time ( $\tau_d$ ) is defined as the time of the inverse course. The former and the latter are determined as 40.7 and 27.1 ms, respectively. Because  $\text{Cs}_3\text{Bi}_2\text{I}_6\text{Br}_3$ -based photodetectors are not affected by the PPC effect, the response speed of our detector is obviously superior to that of the metal-oxide-based UV photodetectors.<sup>5,7</sup> Even among lead-free perovskite-based photodetectors, it is still competitive.<sup>27,34</sup> In fact, the actual response speed of the photodetector should be faster than the results due to the limitation of the reaction time of the switching light source time. As illustrated in Figure 4d, the  $\text{Cs}_3\text{Bi}_2\text{I}_6\text{Br}_3$ -based photodetectors were radiated for hundreds of on-off cycles at ambient conditions. The obtained photocurrents showed a negligible decrease, indicating that the  $\text{Cs}_3\text{Bi}_2\text{I}_6\text{Br}_3$ -based photodetector has a repeatable, stable response with good electrical stability.

To further investigate the reliability of our  $\text{Cs}_3\text{Bi}_2\text{I}_6\text{Br}_3$ -based devices, the long-term stability of the devices and the full-inorganic perovskite film were tested, and the results are shown in Figure 5. Here, it should be noted that our device and perovskite film are without any encapsulation and stay in an ambient environment with the humidity of 25–40% and the temperature around 25 °C. As shown in Figure 5a, the photocurrent of the  $\text{Cs}_3\text{Bi}_2\text{I}_6\text{Br}_3$ -based photodetector drops from 4.56 to 4.4 mA after 100 days, maintaining over 96% of the original value, which indicates the excellent stability of the devices. Meanwhile, to discriminate the stability of the core perovskite film, the absorption of the  $\text{Cs}_3\text{Bi}_2\text{I}_6\text{Br}_3$  film characterized by the UV-vis spectrometer shows negligible change after storage of 100 days in ambient conditions (Figure 5b). This exhibits the high stability of our Cs Bi I Br films and herein accounts for the remarkable stability of the corresponding devices. Besides, Figure S8 shows the typical absorption spectra of the pristine and the aged  $\text{Cs}_3\text{Bi}_2\text{I}_{9-x}\text{Br}_x$  films with  $x = 0, 3$ , and 9 after storage of 100 days. The aged films show negligible degradation in absorbance under the ambient environment. This shows that our  $\text{Cs}_3\text{Bi}_2\text{I}_{9-x}\text{Br}_x$  films are highly stable in an ambient atmosphere.

## CONCLUSIONS

In summary, we successfully synthesized a series of full-inorganic  $\text{Cs}_3\text{Bi}_2\text{I}_{9-x}\text{Br}_x$  perovskite films by varying  $x$  and investigated their optoelectronic property variations along with the evolution of their phase structures and film morphologies. A highly crystalline and continuous flat film of the  $\text{Cs}_3\text{Bi}_2\text{I}_{9-x}\text{Br}_x$  perovskites with  $x$  changing from 3 to 9 can be obtained, and  $\text{Cs}_3\text{Bi}_2\text{I}_6\text{Br}_3$  owns the best photodetecting performance among them. The performance of the  $\text{Cs}_3\text{Bi}_2\text{I}_6\text{Br}_3$ -based photodetectors was studied including responsivity, photosensitivity, detectivity, on/off speed, etc. The  $\text{Cs}_3\text{Bi}_2\text{I}_6\text{Br}_3$ -based photodetector shows a short-circuit current of 4.5  $\mu\text{A}$  and an open-circuit voltage of 0.61 V under the illumination with the white light of 75 mW/cm<sup>2</sup> intensity, demonstrating that it is a typical self-powered device. At the zero bias, the average photocurrent value is 4.7  $\mu\text{A}$ , while the dark current is 145 pA. The photosensitivity reaches  $4.1 \times 10^4$  at the zero bias. Its responsivity and detectivity reach 15 mA/W and  $4.6 \times 10^{11}$  Jones, respectively. Besides, the response and decay duration for the device are as low as 40.7 and 27.1 ms, respectively. More interestingly, the full-inorganic perovskite photodetectors exhibit



excellent stability in the ambient environment and can maintain over 96% of the initial value after 100 days, which is attributed to the high stability of the core perovskite film. The  $\text{Cs}_3\text{Bi}_2\text{I}_6\text{Br}_3$  reported in this paper definitely offers an alternative and promising strategy for the design of future commercial photodetectors with such merits

## EXPERIMENTAL SECTION

**Materials.** All reagents and materials were purchased from Sigma- Aldrich or Alfar Aesar and used as received without any further purification. Indium tin oxide coated glass (ITO glass) and bare glass were bought from Shenzhen Lihe Thin Film Co. Ltd.

**Film Preparation and Characterization.** To synthesize the series of  $\text{Cs}_3\text{Bi}_2\text{I}_{9-x}\text{Br}_x$  perovskite films with  $x$  ranging from 0 to 9, 10 kinds of precursor solutions were prepared according to the stoichiometric composition of each element, with specific information shown in Table S1. The blended powder was added to a mixed solvent of dimethylformamide (DMF) and dimethyl sulfoxide (DMSO) in a ratio of 4:1 and then stirred overnight in a  $\text{N}_2$  glovebox at room temperature. Simultaneously, the ITO glass or the bare glass was ultrasonically washed with deionized water, acetone, isopropanol, and ethanol successively in a duration of 15 min and then dried with nitrogen gas, followed by the treatment of ozone plasma for 20 min. The series of films were deposited on the clean substrates via spin-coating the above precursor solutions at a speed of 3500 rpm for 50 s in a  $\text{N}_2$  glovebox, followed by postannealing at 200 °C for 10 min.

X-ray diffraction (XRD) spectra were collected using a Rigaku MiniFlex600 X-ray diffractometer ( $\text{Cu K}\alpha$ , 1.5406 Å). The absorption spectra were obtained from a UV–vis–NIR spectrometer (Perkin Elmer, Lambda 950). The top-view and cross-sectional morphology of the perovskite films were analyzed by a TESCAN MIRA3 scanning electron microscope. The UPS and X-ray photoelectron spectroscopy (XPS) measurements were performed on ESCALAB 250Xi, Thermo Fisher (using an Al  $\text{K}\alpha$  X-ray source) under a high vacuum ( $10^{-9}$  mbar). For work function measurement with UPS, 10 V bias was applied and Au as a reference.

**Device Fabrication and Characterization.** The patterned ITO glass substrates were cleaned in an ultrasonic bath using detergent, deionized water, ethanol, acetone, and isopropanol for 20 min, respectively. Then, they were treated with UV-ozone plasma in a duration of 20 min. After that, the clean ITO substrate was coated with the PEDOT:PSS thin film with a thickness of around 30 nm at a spin speed of 6000 rpm for 30 s in the ambient environment, followed by 140 °C postannealing for 10 min.

After that, the  $\text{Cs}_3\text{Bi}_2\text{I}_{9-x}\text{Br}_x$  perovskite precursor solution was spin-coated on the substrate at a speed of 3500 rpm for 50 s and then annealed at 200 °C for 10 min under ambient conditions. Finally, the device was formed by thermal evaporating  $\text{C}_{60}$  (25 nm), BCP (8 nm), and Ag (100 nm) on the surface of the  $\text{Cs}_3\text{Bi}_2\text{I}_{9-x}\text{Br}_x$  perovskite film successively.

Electrical and photocurrent measurements were carried out by a semiconductor characterization system (Keithley 4200-SCS) integrated with a monochromatic system (Omin-I3005) and light source (LSH-500). The I–V curves were measured with a sweep voltage from –0.5 to 0.8 V with a step of 0.01 V in the dark or under the illumination of the white light or monochromatic light. The spectral response of the photodetectors was measured with wavelengths from UV to visible (300–600 nm) at a zero bias. The time-dependent photoresponse curves of the device were measured using a chopper to turn on/off the uniformly adjustable semiconductor characterization system under the voltage of 0 V with an interval of 10 s. The devices were covered with some typical mask with an aperture area of 3.14 mm<sup>2</sup>, and all of the measurements were done after exposure of the device to the atmosphere under ambient conditions.

## REFERENCES

- (1) Razeghi, M.; Rogalski, A. Semiconductor Ultraviolet Detectors. *J. Appl. Phys.* 1996, 79, 7433–7473.
- (2) Tian, W.; Lu, H.; Li, L. Nanoscale Ultraviolet Photodetectors Based on One Dimensional Metal Oxide Nanostructures. *Nano Res.* 2015, 8, 382–405.
- (3) Sang, L.; Liao, M.; Sumiya, M. A Comprehensive Review of Semiconductor Ultraviolet Photodetectors: from Thin Film to One- Dimensional Nanostructures. *Sensors* 2013, 13, 10482–10518.
- (4) You, D.; Xu, C.; Zhao, J.; Qin, F.; Zhang, W.; Wang, R.; Shi, Z.; Cui, Q. Single-Crystal ZnO/AlN Core/Shell Nanowires for Ultraviolet Emission and Dual-Color Ultraviolet Photodetection. *Adv. Opt. Mater.* 2019, 7, No. 1801522.

- (5) Liu, X.; Gu, L.; Zhang, Q.; Wu, J.; Long, Y.; Fan, Z. All-printable Band-edge Modulated ZnO Nanowire Photodetectors with Ultra-high Detectivity. *Nat. Commun.* 2014, 5, No. 4007.
- (6) Zheng, Z.; Gan, L.; Li, H.; Ma, Y.; Bando, Y.; Golberg, D.; Zhai, T. A Fully Transparent and Flexible Ultraviolet-Visible Photodetector Based on Controlled Electrospun ZnO-CdO Heterojunction Nano- fiber Arrays. *Adv. Funct. Mater.* 2015, 25, 5885–5894.
- (7) Tian, W.; Zhai, T.; Zhang, C.; Li, S. L.; Wang, X.; Liu, F.; Liu, D.; Cai, X.; Tsukagoshi, K.; Golberg, D.; Bando, Y. Low-cost Fully Transparent Ultraviolet Photodetectors Based on Electrospun ZnO- SnO<sub>2</sub> Heterojunction Nanofibers. *Adv. Mater.* 2013, 25, 4625–4630.
- (8) Zhao, B.; Wang, F.; Chen, H.; Zheng, L.; Su, L.; Zhao, D.; Fang, X. An Ultrahigh Responsivity (9.7 mA W<sup>-1</sup>) Self-Powered Solar-Blind Photodetector Based on Individual ZnO-Ga<sub>2</sub>O<sub>3</sub> Heterostructures. *Adv. Funct. Mater.* 2017, 27, No. 1700264.
- (9) Game, O.; Singh, U.; Kumari, T.; Banpurkar, A.; Ogale, S. ZnO(N)-Spiro-MeOTAD Hybrid Photodiode: An Efficient Self-powered Fast-response UV (visible) Photosensor. *Nanoscale* 2014, 6, 503–513.
- (10) Zhang, D.; Liu, C.; Yin, B.; Xu, R.; Zhou, J.; Zhang, X.; Ruan, S. Organics Filled One-dimensional TiO<sub>2</sub> Nanowires Array Ultraviolet Detector with Enhanced Photo-conductivity and Dark-resistivity. *Nanoscale* 2017, 9, 9095–9103.
- (11) Chong, H.; Wei, G.; Hou, H.; Yang, H.; Shang, M.; Gao, F.; Yang, W.; Shen, G. High-performance Solar-blind Ultraviolet Photodetector Based on Electrospun TiO<sub>2</sub>-ZnTiO<sub>3</sub> Heterojunction Nanowires. *Nano Res.* 2015, 8, 2822–2832.
- (12) Zheng, L.; Yu, P.; Hu, K.; Teng, F.; Chen, H.; Fang, X. Scalable-Production, Self-Powered TiO<sub>2</sub> Nanowell-Organic Hybrid UV Photodetectors with Tunable Performances. *ACS Appl. Mater. Interfaces* 2016, 8, 33924–33932.
- (13) He, Z.; Liu, Q.; Hou, H.; Gao, F.; Tang, B.; Yang, W. Tailored Electrospinning of WO<sub>3</sub> Nanobelts as Efficient Ultraviolet Photo- detectors with Photo-Dark Current Ratios up to 1000. *ACS Appl. Mater. Interfaces* 2015, 7, 10878–10885.
- (14) Kang, J.-H.; Johar, M. A.; Alshehri, B.; Dogheche, E.; Ryu, S.- W. Facile Growth of Density- and Diameter-controlled GaN Nanobridges and Their Photodetector Application. *J. Mater. Chem. C* 2017, 5, 11879–11884.
- (15) Li, D.; Jiang, K.; Sun, X.; Guo, C. AlGaIn Photonics: Recent Advances in Materials and Ultraviolet Devices. *Adv. Opt. Photonics* 2018, 10, No. 43.
- (16) Jiang, H. X.; Lin, J. Y. Percolation Transition of Persistent Photoconductivity in II-VI Mixed Crystals. *Phys. Rev. Lett.* 1990, 64, 2547–2550.
- (17) Lany, S.; Zunger, A. Anion Vacancies as A Source of Persistent Photoconductivity in II-VI and Chalcopyrite Semiconductors. *Phys. Rev. B* 2005, 72, No. 035215.
- (18) Jeon, S.; Ahn, S. E.; Song, I.; Kim, C. J.; Chung, U. I.; Lee, E.; Yoo, I.; Nathan, A.; Lee, S.; Ghaffarzadeh, K.; Robertson, J.; Kim, K. Gated Three-terminal Device Architecture to Eliminate Persistent Photoconductivity in Oxide Semiconductor Photosensor Arrays. *Nat. Mater.* 2012, 11, 301–305.
- (19) Stranks, S. D.; Eperon, G. E.; Grancini, G.; Menelaou, C.; Alcocer, M. J.; Leijtens, T.; Herz, L. M.; Petrozza, A.; Snaith, H. J. Electron-hole Diffusion Lengths Exceeding 1 Micrometer in An Organometal Trihalide Perovskite Absorber. *Science* 2013, 342, 341– 344.
- (20) Gratzel, M. The Rise of Highly Efficient and Stable Perovskite Solar Cells. *Acc. Chem. Res.* 2017, 50, 487–491.
- (21) Ahmadi, M.; Wu, T.; Hu, B. A Review on Organic-Inorganic Halide Perovskite Photodetectors: Device Engineering and Fundamental Physics. *Adv. Mater.* 2017, 29, No. 1605242.
- (22) Kim, M.; Kim, G.-H.; Lee, T. K.; Choi, I. W.; Choi, H. W.; Jo, Y.; Yoon, Y. J.; Kim, J. W.; Lee, J.; Huh, D.; Lee, H.; Kwak, S. K.; Kim, J. Y.; Kim, D. S. Methylammonium Chloride Induces Intermediate Phase Stabilization for Efficient Perovskite Solar Cells. *Joule* 2019, 3, 2179–2192.
- (23) Lu, H.; Tian, W.; Cao, F.; Ma, Y.; Gu, B.; Li, L. A Self-Powered and Stable All-Perovskite Photodetector-Solar Cell Nanosystem. *Adv. Funct. Mater.* 2016, 26, 1296–1302.



- (24) Min, H.; Kim, M.; Lee, S.-U.; Kim, H.; Kim, G.; Choi, K.; Lee, J. H.; Seok, S. I. Efficient, Stable Solar Cells by Using Inherent Bandgap of  $\alpha$ -phase Formamidinium Lead Iodide. *Science* 2019, 366, 749–753.
- (25) Leung, S. F.; Ho, K. T.; Kung, P. K.; Hsiao, V. K. S.; Alshareef, H. N.; Wang, Z. L.; He, J. H. A Self-Powered and Flexible Organometallic Halide Perovskite Photodetector with Very High Detectivity. *Adv. Mater.* 2018, 30, No. 1704611.
- (26) Shen, L.; Fang, Y.; Wang, D.; Bai, Y.; Deng, Y.; Wang, M.; Lu, Y.; Huang, J. A Self-Powered, Sub-nanosecond-Response Solution-Processed Hybrid Perovskite Photodetector for Time-Resolved Photoluminescence-Lifetime Detection. *Adv. Mater.* 2016, 28, 10794–10800.
- (27) Liu, C. K.; Tai, Q.; Wang, N.; Tang, G.; Loi, H. L.; Yan, F. Sn- Based Perovskite for Highly Sensitive Photodetectors. *Adv. Sci.* 2019, 6, No. 1900751.
- (28) Tan, Z. K.; Moghaddam, R. S.; Lai, M. L.; Docampo, P.; Higler, R.; Deschler, F.; Price, M.; Sadhanala, A.; Pazos, L. M.; Credgington, D.; Hanusch, F.; Bein, T.; Snaith, H. J.; Friend, R. H. Bright Light- emitting Diodes Based on Organometal Halide Perovskite. *Nat. Nanotechnol.* 2014, 9, 687–692.
- (29) Bao, C.; Yang, J.; Bai, S.; Xu, W.; Yan, Z.; Xu, Q.; Liu, J.; Zhang, W.; Gao, F. High Performance and Stable All-Inorganic Metal Halide Perovskite-Based Photodetectors for Optical Communication Applications. *Adv. Mater.* 2018, 30, No. e1803422.
- (30) Zheng, E.; Yuh, B.; Tosado, G. A.; Yu, Q. Solution-processed Visible-blind UV Photodetectors Based on  $\text{CH}_3\text{NH}_3\text{PbCl}_3$  Perovskite Thin Films. *J. Mater. Chem. C* 2017, 5, 3796–3806.
- (31) Waleed, A.; Tavakoli, M. M.; Gu, L.; Wang, Z.; Zhang, D.; Manikandan, A.; Zhang, Q.; Zhang, R.; Chueh, Y. L.; Fan, Z. Lead-Free Perovskite Nanowire Array Photodetectors with Drastically Improved Stability in Nanoengineering Templates. *Nano Lett.* 2017, 17, 523–530.
- (32) Tong, X. W.; Kong, W. Y.; Wang, Y. Y.; Zhu, J. M.; Luo, L. B.; Wang, Z. H. High-Performance Red-Light Photodetector Based on Lead-Free Bismuth Halide Perovskite Film. *ACS Appl. Mater. Interfaces* 2017, 9, 18977–18985.
- (33) Wu, C.; Du, B.; Luo, W.; Liu, Y.; Li, T.; Wang, D.; Guo, X.; Ting, H.; Fang, Z.; Wang, S.; Chen, Z.; Chen, Y.; Xiao, L. Highly Efficient and Stable Self-Powered Ultraviolet and Deep-Blue Photodetector Based on  $\text{Cs}_2\text{AgBiBr}_6/\text{SnO}_2$  Heterojunction. *Adv. Opt. Mater.* 2018, 6, No. 1800811.
- (34) Hussain, A. A.; Rana, A. K.; Ranjan, M. Air-stable Lead-free Hybrid Perovskite Employing Self-powered Photodetection with An Electron/hole-conductor-free Device Geometry. *Nanoscale* 2019, 11, 1217–1227.
- (35) Wang, Y.; Dar, M. I.; Ono, L. K.; Zhang, T.; Kan, M.; Li, Y.; Zhang, L.; Wang, X.; Yang, Y.; Gao, X.; Qi, Y.; Gratzel, M.; Zhao, Y. Thermodynamically Stabilized  $\beta$ - $\text{CsPbI}_3$ -based Perovskite Solar Cells with Efficiencies > 18%. *Science* 2019, 365, 591–595.
- (36) Ghosh, B.; Wu, B.; Mulmudi, H. K.; Guet, C.; Weber, K.; Sum, T. C.; Mhaisalkar, S.; Mathews, N. Limitations of  $\text{Cs}_3\text{Bi}_2\text{I}_9$  as Lead-Free Photovoltaic Absorber Materials. *ACS Appl. Mater. Interfaces* 2018, 10, 35000–35007.
- (37) Yu, B.-B.; Liao, M.; Yang, J.; Chen, W.; Zhu, Y.; Zhang, X.; Duan, T.; Yao, W.; Wei, S.-H.; He, Z. Alloy-induced Phase Transition and Enhanced Photovoltaic Performance: The Case of  $\text{Cs}_3\text{Bi}_2\text{I}_{9-x}\text{Br}_x$  Perovskite Solar Cells. *J. Mater. Chem. A* 2019, 7, 8818–8825.
- (38) Hodgkins, T. L.; Savory, C. N.; Bass, K. K.; Seckman, B. L.; Scanlon, D. O.; Djurovich, P. I.; Thompson, M. E.; Melot, B. C. Anionic Order and Band Gap Engineering in Vacancy Ordered Triple Perovskites. *Chem. Commun.* 2019, 55, 3164–3167.
- (39) McCall, K. M.; Stoumpos, C. C.; Kontsevoi, O. Y.; Alexander, G. C. B.; Wessels, B. W.; Kanatzidis, M. G. From 0D  $\text{Cs}_3\text{Bi}_2\text{I}_9$  to 2D  $\text{Cs}_3\text{Bi}_2\text{I}_6\text{Cl}_3$ : Dimensional Expansion Induces a Direct Band Gap but Enhances Electron–Phonon Coupling. *Chem. Mater.* 2019, 31, 2644–2650.
- (40) Park, B. W.; Philippe, B.; Zhang, X.; Rensmo, H.; Boschloo, G.; Johansson, E. M. Bismuth Based Hybrid Perovskites  $\text{A}_3\text{Bi}_2\text{I}_9$  (A: Methylammonium or Cesium) for Solar Cell Application. *Adv. Mater.* 2015, 27, 6806–6813.
- (41) Bai, F.; Hu, Y.; Hu, Y.; Qiu, T.; Miao, X.; Zhang, S. Lead-free, Air-stable Ultrathin  $\text{Cs}_3\text{Bi}_2\text{I}_9$  Perovskite Nanosheets for Solar Cells. *Sol. Energy Mater. Sol. Cells* 2018, 184, 15–21.

- (42) Bresolin, B.-M.; Balayeva, N. O.; Granone, L. I.; Dillert, R.; Bahnemann, D. W.; Sillanpää, M. Anchoring Lead-free Halide  $\text{Cs}_3\text{Bi}_2\text{I}_9$  Perovskite on UV100-TiO<sub>2</sub> for Enhanced Photocatalytic Performance. *Sol. Energy Mater. Sol. Cells* 2020, 204, No. 110214.
- (43) Sze, S. M.; Ng, K. K. *Photodetectors and Solar Cells. Physics of Semiconductor Devices*; Wiley, 2006; pp 663–742.
- (44) Xiu, J.; Shao, Y.; Chen, L.; Feng, Y.; Dai, J.; Zhang, X.; Lin, Y.; Zhu, Y.; Wu, Z.; Zheng, Y.; Pan, H.; Liu, C.; Shi, X.; Cheng, X.; He, Z. Defining The Composition and Electronic Structure of Large-scale and Single-crystalline Like  $\text{Cs}_2\text{AgBiBr}_6$  Films Fabricated by Capillary- assisted Dip-coating Method. *Mater. Today Energy* 2019, 12, 186– 197.
- (45) Cao, F.; Tian, W.; Gu, B.; Ma, Y.; Lu, H.; Li, L. High- performance UV–vis Photodetectors Based on Electrospun ZnO Nanofiber Solution Processed Perovskite Hybrid Structures. *Nano Res.* 2017, 10, 2244–2256.
- (46) Sun, J.; Zhang, Z.; Li, X.; Qin, H.; Sun, Y.; Cai, Y.; Yu, G.; Zhang, Z.; Zhang, J.; Shangguan, Y.; Jin, L.; Li, X.; Zhang, B.; Popov, V. V. Two-terminal Terahertz Detectors Based on AlGaIn/GaN High- electron-mobility Transistors. *Appl. Phys. Lett.* 2019, 115, No. 111101.

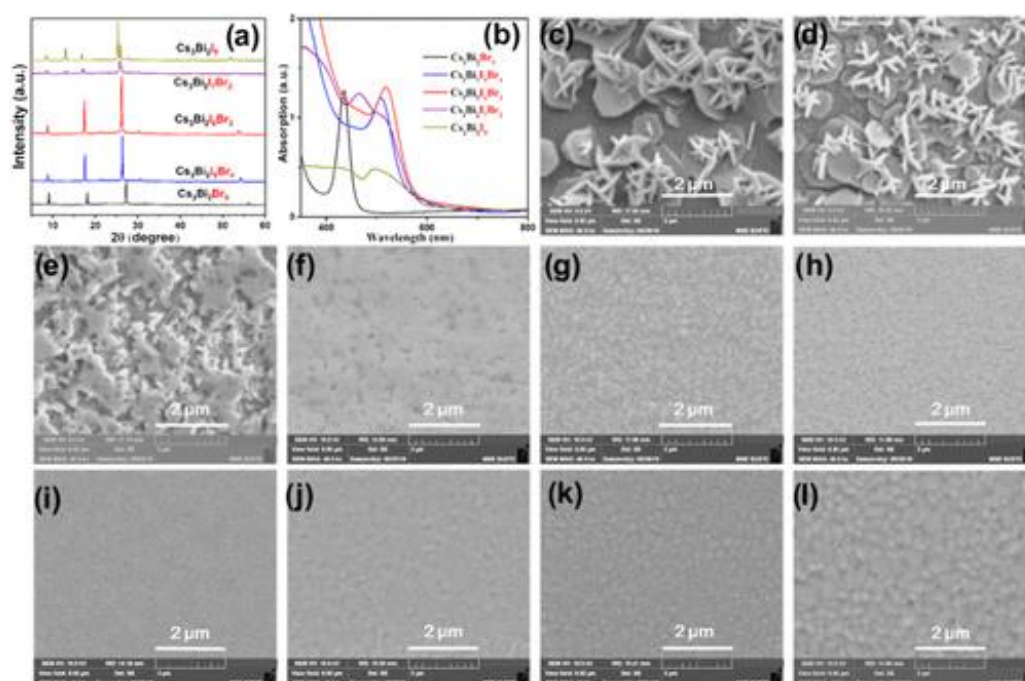


Figure 1. XRD patterns (a) and absorption spectra (b) of some typical  $\text{Cs}_3\text{Bi}_2\text{I}_{9-x}\text{Br}_x$  films with x equal to 0, 2, 3, 4, and 9. (c) (l) Topographic scanning electron microscopy (SEM) images of the  $\text{Cs}_3\text{Bi}_2\text{I}_{9-x}\text{Br}_x$  films with x equal to 0, 1, 2, 3, 4, 5, 6, 7, 8, and 9.

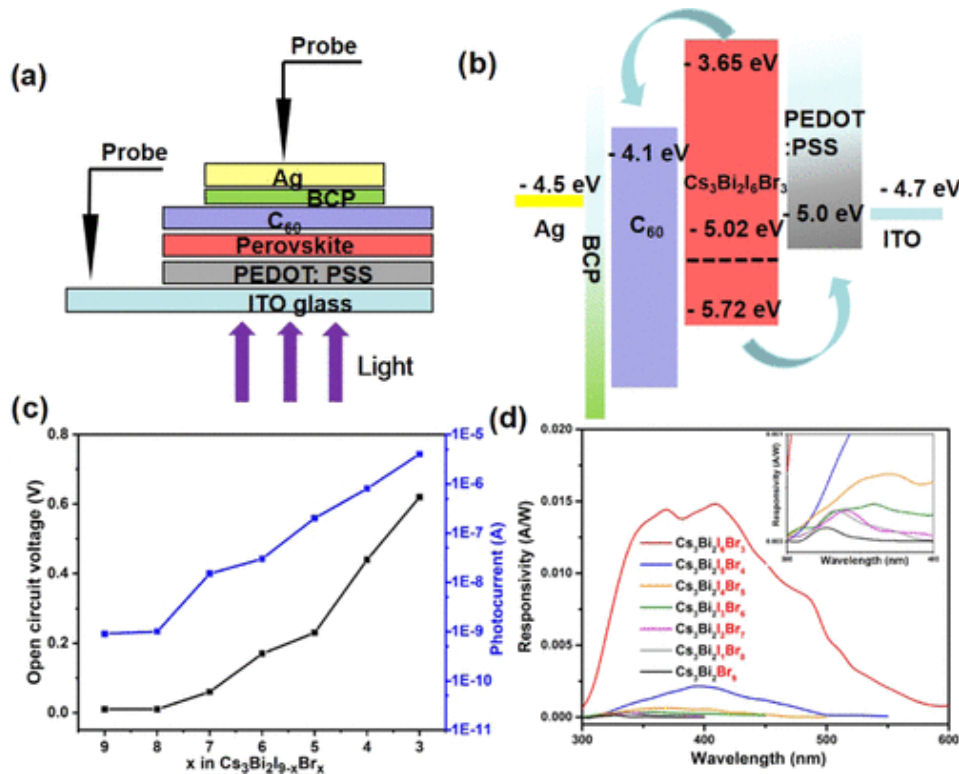


Figure 2. (a) Device configuration of the  $Cs_3Bi_2I_{9-x}Br_x$ -based photodetectors. (b) Energy-level diagram of the  $Cs_3Bi_2I_6Br_3$ -based device. (c) Open-circuit voltage (black line) and the short-circuit current (blue line). (d) Responsivity of  $Cs_3Bi_2I_{9-x}Br_x$ -based photodetectors with  $x$  equal to 3, 4, 5, 6, 7, 8, and 9, respectively.

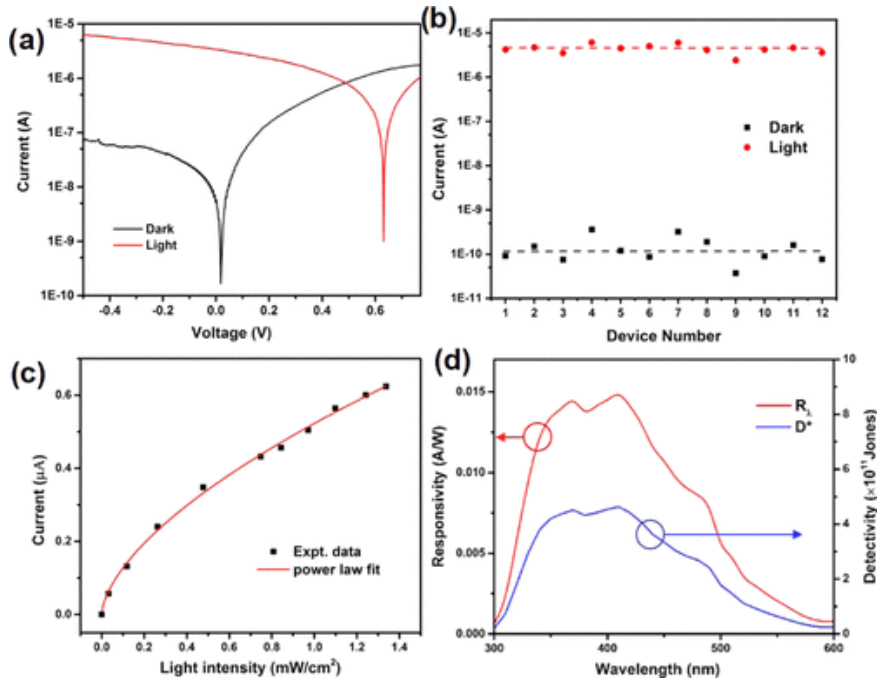


Figure 3. (a)  $I$ - $V$  characteristics of the  $Cs_3Bi_2I_6Br_3$ -based photodetector under dark and white light illumination of an intensity of 75  $mW/cm^2$ . (b) Statistics of the dark current and the photocurrent of 12 devices in a batch. (c) Power law fitting of the

relationship between the photocurrent and the incident light intensity. (d) Responsivity and detectivity of the  $\text{Cs}_3\text{Bi}_2\text{I}_6\text{Br}_3$ -based photodetector.

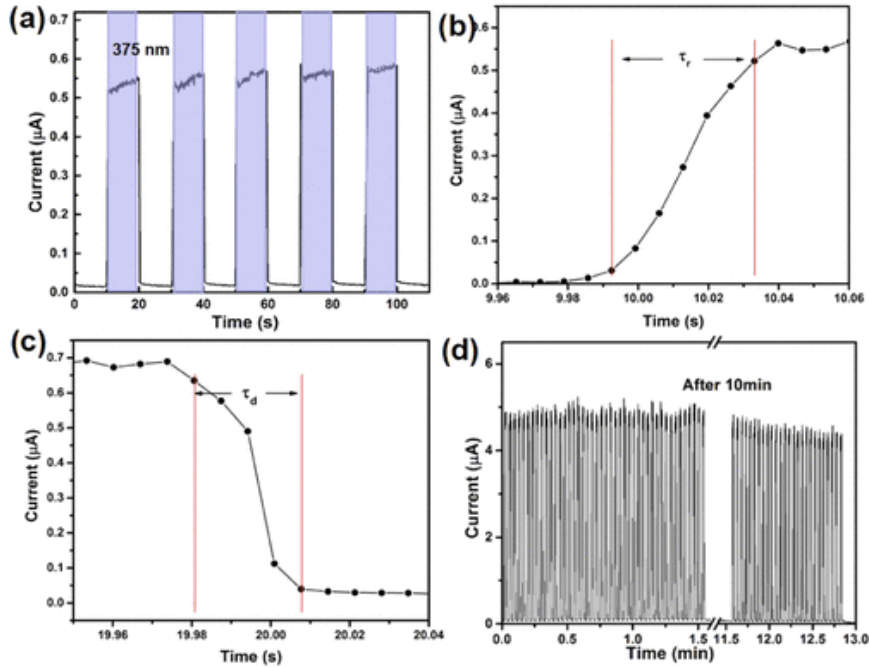


Figure 4. (a) Time-dependent on/off photoswitching test of the  $\text{Cs}_3\text{Bi}_2\text{I}_6\text{Br}_3$ -based photodetector with the illumination wavelength of 375 nm at a zero bias. (b) “On” and (c) “off” edge to determine the response and decay duration. (d) Forty-five cycles of photoswitching test, followed by the other 25 cycles with an interval of 10 min of light soaking.

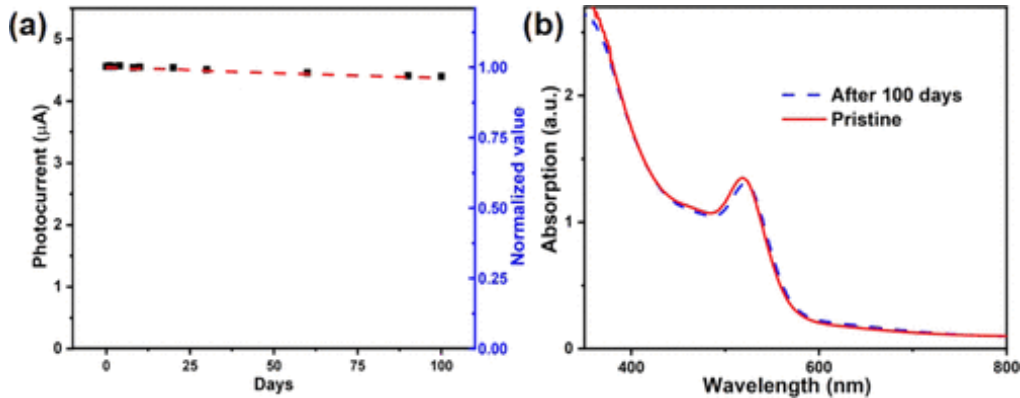


Figure 5. Shelf-life test of the  $\text{Cs}_3\text{Bi}_2\text{I}_6\text{Br}_3$ -based photodetectors: (a) photocurrent evolution of the devices after storage of 100 days and (b) absorption spectra of the pristine and the aged  $\text{Cs}_3\text{Bi}_2\text{I}_6\text{Br}_3$  films after storage of 100 days.

